Transient growth analysis of flow through a sudden expansion in a circular pipe

C. D. Cantwell* and D. Barkley†

Mathematics Institute and Centre for Scientific Computing, University of Warwick, UK

H. M. Blackburn‡

Department of Mechanical and Aerospace Engineering, Monash University, Australia

(Dated: July 18, 2009)

Abstract

Results are presented from a numerical study of transient growth experienced by infinitesimal perturbations to flow in an axisymmetric pipe with a sudden 1:2 diametral expansion. First, the downstream reattachment point of the steady laminar flow is accurately determined as a function of Re and it is established that the flow is linearly stable up to Re=1400. A direct method is used to calculate the optimal transient energy growth for specified time horizon τ, Re up to 1200, and low-order azimuthal wavenumber m. The critical Re for the onset of growth with different m is determined. At each Re the maximum growth is found in azimuthal mode m=1 and this maximum is found to increase exponentially with Re. The time evolution of optimal perturbations is presented and shown to correspond to sinuous oscillations of the shear layer. Sub-optimal perturbations are presented and discussed. Finally, full three-dimensional DNS with the inflow perturbed with Gaussian white-noise confirms the presence of the structures determined by the transient growth analysis.

PACS numbers: 47.27.nf, 47.20.Ft, 47.15.Fe,

Keywords: transient growth, convective instability, pipe flow, sudden expansion

*Email: c.d.cantwell@warwick.ac.uk

†Email: d.barkley@warwick.ac.uk

‡Email: hugh.blackburn@eng.monash.edu.au

I. INTRODUCTION

The dynamics of flow through abrupt geometrical expansions is of both practical importance and fundamental interest. The axisymmetric expansion[1–6], in particular, is a primitive geometry occurring in numerous engineering and industrial settings. It is also relevant to bio-medical applications as a model of flow through arterial stenoses[7–11]. At a fundamental level this geometry, together with the closely related planar expansion[12–14] and backward-facing step[15? –18], serve as prototypes for understanding the dynamics of flow separation. Over the past four decades studies of these flows have addressed issues such as reattachment lengths[1], symmetry breaking[5], and time-dependence[20].

The focus of this paper is the transient linear dynamics of the 1 to 2 axisymmetric expansion. We show that for values of the Reynolds numbers well below any linear instability, the flow strongly amplifies infinitesimal inlet perturbations. We argue that transient linear amplification is a potentially more important effect in this flow than linear instability.

Much of the previous research on the axisymmetric expansion has concentrated on the steady, laminar flow regime and the accurate determination of the separation and subsequent reattachment. Both experimental[1–5,19,20] and computational[19,21,22] studies find that the reattachment length varies linearly with Reynolds number in the steady regime, with the proportionality depending on whether the inlet flow is a flat profile or a fully developed Hagen–Poiseuille profile[23]. Separation and reattachment in the turbulent regime has also been studied[12,24].

Recent and carefully controlled experiments by Mullin *et al.*[5] on the 1 to 2 expanding pipe flow with a fully developed inlet profile report a steady-state breaking of axisymmetry at $Re = 1139 \pm 10$. The Reynolds number is defined in terms of the inlet diameter and bulk velocity. This symmetry breaking is the rotational analog of the symmetry breaking observed in the symmetric planar expansion[13,14,25]. However, in the planar case there is now general agreement between computation and experiment on the bifurcation, while in the axisymmetric case, linear stability computations by Hall *et al.*[26] (also verified in the present study) find that there is no bifurcation of the perfectly symmetric problem at Reynolds numbers comparable to those reported in the experiments[5].

Many experimental studies report unsteadiness and oscillations in the expanding-pipe flow[1,5,20,27,28]. There is, however, no agreement as to the Reynolds number at which oscilla-

tions first arise. The explanation for the discrepancy has been attributed to the sensitivity of the expansion to the inlet profile[4,22,23].

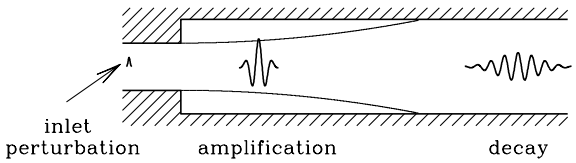

FIG. 1: Sketch illustrating the evolution of a perturbation through an expanding pipe. Small inlet perturbations are amplified in the region of the separated axisymmetric shear layer, but eventurally decay downstream. Hence, even though the flow is linearly stable, it supports very strong transient growth of perturbations.

The aim of this paper is to quantify and highlight the importance of transient growth of infinitesimal perturbations in expanding pipe flow. Fig. 1 illustrates the essential idea. Small disturbances in the inlet upstream of the expansion are amplified in the region containing the separated axisymmetric shear layer following the expansion. The amplified disturbances are then advected into the downstream pipe where they inevitably decay. This leads to a situation in which the flow may be highly sensitive to incoming perturbations, but only transiently. Hence, even though the flow is linearly stable, in that all perturbations eventually decay and likewise all eigenvalues are negative, the flow may be highly susceptible to small perturbations. From a local perspective one would attribute the transient dynamics to a localized region of convective instability within the flow resulting from an inflectional velocity profile[29–31]. In the context of a direct numerical study where one does not resort to local parallel approximations but instead fully resolves all aspects of the flow, one understands and analyzes the transient dynamics as a transient growth problem or equivalently as a singular value problem. For example, recent studies have highlighted the importance of transient dynamics due to localized regions of convective instability for the backward-facing step[15], curved channel flow[15,32] and steady and pulsatile stenotic flow[8]. This is the approach taken in the present work.

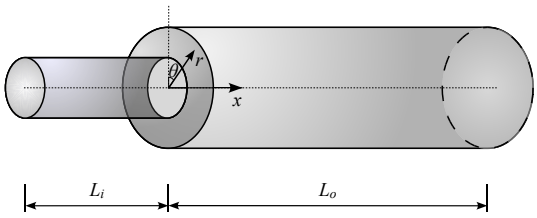

FIG. 2: Geometry of the expanding pipe. The computational flow domain Ω is illustrated with the cylindrical coordinate system and the inlet and outlet lengths indicated (not to scale).

II. METHODOLOGY

A. Governing equations and flow geometry

The flow is governed by the incompressible Navier–Stokes equations

$$\partial_t \mathbf{u} + (\mathbf{u} \cdot \nabla)\mathbf{u} = -\nabla p + Re^{-1}\nabla^2 \mathbf{u}, \tag{1a}$$

$$\nabla \cdot \mathbf{u} = 0, \tag{1b}$$

where $\mathbf{u}$ is the fluid velocity and p is the modified or kinematic static pressure. Without loss of generality we have set the density to unity. The equations are written in dimensionless form with the velocity normalized by $\bar{U}$, the bulk velocity of the incoming flow, and lengths normalized by the diameter of the inlet pipe D. Thus the Reynolds number is the bulk Reynolds number of the inlet pipe flow given by $Re = \bar{U}D/\nu$, where ν the fluid's kinematic viscosity.

To avoid possible confusion when reading the following material it is useful to emphasize here the approach taken to non-dimensionalization. Except where indicated otherwise, all quantities reported employ the normalization used above in defining the Reynolds number. In particular this means that lengths are presented in terms of the inlet pipe diameter, D. The exception we make to this rule is in recording downstream reattachment points, where step height $h = D/2$ is also used as a measure of length. This exception is made to facilitate comparison to previous works. Throughout the paper, times are in units of $D/\bar{U}$.

The pipe geometry naturally lends itself to using cylindrical coordinates which are denoted (x, r, θ). Here x is used for the axial coordinate since this corresponds to the streamwise direction, with $x = 0$ at the expansion location. The fluid velocity in these cylindrical coordinates is thus written $\mathbf{u} = (u_x, u_r, u_\theta)$.

Ideally the flow geometry would be infinite in the streamwise direction. In practice, the computational flow domain Ω consists of a finite inflow region of length L_i upstream of the expansion and a finite outflow region of length L_o downstream of the expansion as in Fig. 2. For sufficiently large L_i and L_o, as used in this study, results are independent of these lengths and the flow approximates the infinite case.

We impose a fully developed Hagen–Poiseuille incoming profile, which in non-dimensional form is given by $\mathbf{u} = 2(1 - 4r^2)\mathbf{e}_x$. We use no-slip boundary conditions on all walls of the pipe and impose a stress-free outflow boundary condition at the downstream end of the pipe. Thus the boundary conditions for the flow problem are

$$\mathbf{u}(\partial\Omega_i, t) = 2(1 - 4r^2)\mathbf{e}_x, \tag{2a}$$

$$\mathbf{u}(\partial\Omega_w, t) = \mathbf{0}, \tag{2b}$$

$$\mathbf{e}_x \cdot \nabla\mathbf{u}(\partial\Omega_o, t) = \mathbf{0}, \quad p(\partial\Omega_o, t) = 0, \tag{2c}$$

where $\partial\Omega_i$ is the inlet boundary at $x = -L_i$, $\partial\Omega_w$ is the boundary corresponding to the rigid walls of the inlet pipe, outlet pipe and expansion, and $\partial\Omega_o$ is the outlet boundary at $x = L_o$. Variations on these boundary conditions will appear in the stability and transient growth problems as well as for studies of noisy inflow and will be discussed at the appropriate place.

B. Linear stability and transient growth problems

We briefly summarize the main aspects of the linear stability and transient growth problems. Some further details for the particular problem are given in Sec. II C. General accounts of the time-stepper approach used here may be found elsewhere[33,34].

The first step in the analysis is to obtain base flows $\mathbf{U}$. In this study these are steady, two-dimensional, axisymmetric solutions to Eqs. (1) of the form $\mathbf{U} = (U_x(x, r), U_r(x, r), 0)$. For the range of Re considered in this paper, these solutions are unique functions of Re.

The next step is to consider the evolution of infinitesimal disturbances $\mathbf{u}'$ to the base flow. These are governed by the linearized Navier–Stokes equations

$$\partial_t\mathbf{u}' + \mathbf{DN} \cdot \mathbf{u}' = -\nabla p' + Re^{-1}\nabla^2\mathbf{u}', \tag{3a}$$

$$\nabla \cdot \mathbf{u}' = 0, \tag{3b}$$

where

$$\mathbf{DN} \cdot \mathbf{u}' \equiv (\mathbf{U} \cdot \nabla)\mathbf{u}' + (\mathbf{u}' \cdot \nabla)\mathbf{U} \tag{4}$$

The boundary conditions for Eqs. (3) will be addressed at the end of Sec. II C.

The linear evolution of a perturbation from $t = 0$ to a later time t under Eqs. (3) can be expressed eloquently as the action of a linear state transition operator $\mathcal{A}(t)$ on the initial perturbation $\mathbf{u}'(0)$ as

$$\mathbf{u}'(t) = \mathcal{A}(t)\mathbf{u}'(0). \tag{5}$$

We then perform an analysis, either of stability or of transient growth, for this linear evolution operator.

For linear stability, we seek normal mode solutions of the form $\mathbf{u}'(x, r, \theta, t) = \exp(\sigma_j t)\tilde{\mathbf{u}}_j(x, r, \theta) + \text{c.c.}$, where the $\tilde{\mathbf{u}}_j$ are eigenmodes and the σ_j are eigenvalues. For any fixed arbitrary time T (typically T is of order unity under the scaling we have used) the eigenmodes are solutions of

$$\mathcal{A}(T)\tilde{\mathbf{u}}_j = \mu_j \tilde{\mathbf{u}}_j \tag{6}$$

where the eigenvalues μ_j and σ_j are related by $\mu_j = \exp(\sigma_j T)$. The eigenvalues μ_j of largest modulus are found iteratively by actions of the operator $\mathcal{A}(T)$ as discussed in Sec. II C. If there exist any solutions of Eq. (6) with $|\mu_j| > 1$, corresponding to σ_j with positive real part, then the base flow $\mathbf{U}$ is linearly unstable.

The transient growth computations consist of determining the greatest possible energy growth, G, over all initial perturbations for a given finite time horizon τ. Because the evolution is linear, it is sufficient to consider initial perturbations with unit norm in the standard L_2 inner product $(\cdot, \cdot)$ over the flow domain Ω. Then the energy of such a perturbation after time τ, relative to the initial energy, is

$$\frac{E(\tau)}{E(0)} = ||\mathbf{u}'(\tau)||^2 = (\mathbf{u}'(\tau), \mathbf{u}'(\tau)),$$

where $||\mathbf{u}'(0)|| = 1$. Using the evolution operator $\mathcal{A}(\tau)$ and its adjoint $\mathcal{A}^*(\tau)$ this can be written as

$$\begin{aligned}\frac{E(\tau)}{E(0)} &= (\mathcal{A}(\tau)\mathbf{u}'(0), \mathcal{A}(\tau)\mathbf{u}'(0)) \\ &= (\mathbf{u}'(0), \mathcal{A}^*(\tau)\mathcal{A}(\tau)\mathbf{u}'(0)).\end{aligned}$$

Let λ_j and $\mathbf{v}_j$ denote eigenvalues and normalized eigenmodes of $\mathcal{A}^*(\tau)\mathcal{A}(\tau)$:

$$\mathcal{A}^*(\tau)\mathcal{A}(\tau)\mathbf{v}_j = \lambda_j \mathbf{v}_j, \qquad ||\mathbf{v}_j|| = 1. \tag{7}$$

Then the maximum growth obtainable at time τ, denoted $G(\tau)$, is

$$G(\tau) \equiv \max_{||\mathbf{u}'(0)||=1} \frac{E(\tau)}{E(0)} = \max_j \lambda_j. \tag{8}$$

Thus the maximum growth is obtained by computing the dominant eigenvalue, and corresponding eigenmode, of $\mathcal{A}^*(\tau)\mathcal{A}(\tau)$. This is again done iteratively through actions of $\mathcal{A}^*(\tau)\mathcal{A}(\tau)$ as discussed in Sec. II C.

Finding the dominant eigenvalues of $\mathcal{A}^*(\tau)\mathcal{A}(\tau)$ is equivalent to finding the largest singular values of $\mathcal{A}(\tau)$. The eigenmode $\mathbf{v}_j$ in Eq. (7) provides an initial perturbation $\mathbf{u}'(0)$ which generates a growth λ_j over time τ. Referring to Fig. 1, this is the inlet perturbation. Potentially, one is also interested in the evolution of perturbations from $t = 0$ to some large value of t where the perturbation washes out of the system. The evolved perturbation at time τ has a particular meaning however. Defining $\mathbf{u}_j$ to be the normalized perturbation at time τ evolved from initial condition $\mathbf{u}'(0) = \mathbf{v}_j$, we have

$$\mathcal{A}(\tau)\mathbf{v}_j = \sigma_j \mathbf{u}_j, \qquad ||\mathbf{v}_j|| = ||\mathbf{u}_j|| = 1, \tag{9}$$

where $\sigma_j = ||\mathbf{u}'(\tau)||$. This is nothing other than the leading part for the singular value decomposition of $\mathcal{A}(\tau)$.

When solving the eigenvalue problem, the time horizon, denoted T in this case, is set by practical considerations; the eigenvalues λ_j are independent of T. For the transient growth problem, the eigenvalues of $\mathcal{A}^*(\tau)\mathcal{A}(\tau)$, singular values of $\mathcal{A}(\tau)$, depend on the time horizon, here denoted τ, and this value is a parameter of study — each new τ requires a new solution to (7). As is the case for linear stability, in the transient growth problem one is primarily interested in the optimal energy growth given by the dominant eigenvalue of $\mathcal{A}^*(\tau)\mathcal{A}(\tau)$ as these describe the 'most dangerous' cases. However, as we show in Sec. III C the first few sub-dominant eigenvalues can also be of interest.

The final general point is that the eigenmodes of $\mathcal{A}(\tau)$ and $\mathcal{A}^*(\tau)\mathcal{A}(\tau)$ are trigonometric in the azimuthal direction, of the form $\exp(\mathrm{i}m\theta) + \text{c.c.}$, for integer m. Moreover, eigenmodes with different azimuthal mode numbers m decouple. As a result, m effectively becomes a specified input parameter to the stability or transient growth problem. (See Sec. II C). Specifically then, the optimal energy growth is a function not only of the time horizon τ as indicated in Eq. (8), but also the control parameter, Re, and the azimuthal mode number m, i.e. $G = G(\tau, Re, m)$. For clarity, the notation used later in this paper will be restricted to only those dependencies relevant to the context.

C. Further details

For completeness we present further details of the numerical computations used in this study. We employ a time-stepper approach[33] in which all problems are solved with the same code base: a spectral/*hp* element–Fourier discretization of the Navier–Stokes equations[35].

A representative computational mesh is shown in Fig. 3. The axial–radial plane, (x, r), is discretized using a spectral-element mesh as in Fig. 3(a). All meshes used in this study have the same inflow length $L_i = 5$ and the same refinement structure in the vicinity of the expansion. This mesh has been used in previous studies of the planar backward-facing step[8]. The outflow length requirements depend on τ and vary from $L_0 = 25$ (as in Fig. 3) at small τ up to $L_0 = 75$ at τ=130, the largest considered in this study. The longer meshes differ from that shown only by the continuation of regular downstream elements. The requirements for the inflow and outflow lengths are set by the boundary conditions on the transient growth computations discussed shortly.

Velocity components and the pressure are expanded in a tensor product of order-N polynomials within each element. In the azimuthal direction a Fourier representation with complex modes is used to produce the full three-dimensional physical geometry illustrated in Fig. 3(b). A Fourier-mode-dependent set of boundary conditions is imposed at $r = 0$, the centerline of the pipe, as detailed elsewhere[35]. For linear analyses, azimuthal Fourier modes can be dealt with independently, whereas in direct nonlinear simulations of three-dimensional states, Fourier modes must be dealt with concurrently.

The choice of polynomial order for the spectral-element expansion is dictated by the need to resolve the separated shear layer of the base flow. This can be best assessed by analysis of the reattachment of the separating streamline, since its location depends sensitively on the resolution of the separated shear layer, particularly near the separation point. Table I shows the dependence of the flow reattachment point, x_r, on polynomial order at Re=1000. A value of $N = 6$ is sufficient to resolve the flow accurately and this value is used for all computations in this study.

Nonlinear solutions consists of two types. First, there are steady, axisymmetric base flows $\mathbf{U} = (U_x(x, r), U_r(x, r))$. These are computed by time evolving the two-dimensional (axisymmetric) Navier–Stokes equations with boundary conditions given by Eqs. (2) until a steady state is reached. The final flow field is then stored for use with the linear stability

TABLE I: Streamwise position of base flow reattachment point (in units of step height, h) at Re=1000, as a function of spectral-element polynomial order N. The outflow length is $L_o = 75 = 150h$.

Order, N	x_r/h
3	89.3312
4	89.2565
5	89.2655
6	89.2630
7	89.2623
8	89.2620

analysis and growth computations.

The other types of nonlinear solutions presented are fully three-dimensional, time-dependent flows resulting from small disturbances added to the parabolic inflow. Specifically, the transverse velocity components of the inflow are perturbed by a small amount of Gaussian white noise. The boundary conditions, Eq. (2a), are replaced by

$$\mathbf{u}(\partial\Omega_i, t) = 2(1 - 4r^2)\mathbf{e}_x + \eta_r \mathbf{e}_r + \eta_\theta \mathbf{e}_\theta \tag{10}$$

where η_r, η_θ are random variables drawn from a Gaussian distribution with zero mean and standard deviation γ. In most cases we use $\gamma = 10^{-2}$, but also use $\gamma = 2.5 \times 10^{-3}$.

The linear computations (eigenvalues and optimal growth) are based on the time-stepper approach in which the actions of the linear operators $\mathcal{A}$ and $\mathcal{A}^*$ are effected by evolving perturbations in time using a modified version of the same simulation code. This is coupled with standard linear algebra algorithms to obtain the desired eigenvalues and eigenmodes.

Since we work in cylindrical coordinates and the base flows are axisymmetric, the lin-

earized advection operator in Eqs. (3–4) has the following explicit form

$$\mathbf{DN}\cdot\mathbf{u}' = \left[\begin{pmatrix} \mathbf{U}\cdot\nabla & 0 & 0 \\ 0 & \mathbf{U}\cdot\nabla & 0 \\ 0 & 0 & \mathbf{U}\cdot\nabla \end{pmatrix} + \begin{pmatrix} \partial_x U_x & \partial_r U_x & 0 \\ \partial_x U_r & \partial_r U_r & 0 \\ 0 & 0 & U_r/r \end{pmatrix}\right] \begin{pmatrix} u'_x \\ u'_r \\ u'_\theta \end{pmatrix}$$

where $\mathbf{U}\cdot\nabla = U_x\partial_x + U_r\partial_r$. Thus the only non-zero term resulting from cylindrical coordinates is $U_r u'_\theta/r$. All other terms vanish for the base flows we consider or have Cartesian analogs.

Computing the action of $\mathcal{A}^*(\tau)$, necessary for computing the action of $\mathcal{A}^*(\tau)\mathcal{A}(\tau)$, requires evolving perturbations by equations that are adjoint to Eqs. (3). Using integration by parts these adjoint equations are

$$-\partial_t\mathbf{u}^* + \mathbf{DN}^*\cdot\mathbf{u}^* = -\nabla p^* + Re^{-1}\nabla^2\mathbf{u}^* \tag{11a}$$

$$\nabla\cdot\mathbf{u}^* = 0 \tag{11b}$$

where $\mathbf{u}^*$ and p^* are the adjoint velocity and pressure fields, respectively. The adjoint advection terms are

$$\mathbf{DN}^*\cdot\mathbf{u}^* = \left[\begin{pmatrix} -\mathbf{U}\cdot\nabla & 0 & 0 \\ 0 & -\mathbf{U}\cdot\nabla & 0 \\ 0 & 0 & -\mathbf{U}\cdot\nabla \end{pmatrix} + \begin{pmatrix} \partial_x U_x & \partial_x U_r & 0 \\ \partial_r U_x & \partial_r U_r & 0 \\ 0 & 0 & U_r/r \end{pmatrix}\right] \begin{pmatrix} u^*_x \\ u^*_r \\ u^*_\theta \end{pmatrix}$$

The change of sign from $(\mathbf{U}\cdot\nabla)\mathbf{u}'$ to $-(\mathbf{U}\cdot\nabla)\mathbf{u}^*$ follows from one integration by parts, together with the divergence-free condition. The second term is equivalent to a standard matrix transpose. The action of $\mathcal{A}^*(\tau)\mathcal{A}(\tau)$ on a perturbation is obtained by evolving the perturbation forward τ time units under Eqs. (3), followed by evolving the perturbation

backward τ time units under Eqs. (11). This is easy to implement when using the time-stepper approach.

For axisymmetric base flows, the linear operators $\mathcal{A}$ and $\mathcal{A}^*$ are homogeneous in the azimuthal direction and different azimuthal modes decouple. Eqs. (3) and (11) then have invariant subspaces of the form

$$\begin{aligned} u'_x(x,r,\theta,t) &= \hat{u}^m_x(x,r,t)\cos(m\theta) \\ u'_r(x,r,\theta,t) &= \hat{u}^m_r(x,r,t)\cos(m\theta) \\ u'_\theta(x,r,\theta,t) &= \hat{u}^m_\theta(x,r,t)\sin(m\theta) \\ p'(x,r,\theta,t) &= \hat{p}^m(x,r,t)\cos(m\theta) \end{aligned}$$

or similar with any rotation in θ, where m is integer. The time stepping code thus evolves the three velocity components (u'_x, u'_r, u'_θ), on a strictly two-dimensional (x,r) spectral-element mesh. The mode number m is an input parameter.

For computing the eigenvalues of $\mathcal{A}(T)$, the inflow boundary condition is homogeneous Dirichlet, and all other boundary conditions are as in Eqs. (2). For computing eigenvalues of $\mathcal{A}^*(\tau)\mathcal{A}(\tau)$ we use homogeneous Dirichlet boundary conditions on all boundaries both for the operator $\mathcal{A}(\tau)$ and $\mathcal{A}^*(\tau)$. As discussed elsewhere[33], for transient growth problems it is essential that the boundaries be sufficiently far upstream and downstream that perturbations do not reach them during the computation of $\mathcal{A}^*(\tau)\mathcal{A}(\tau)$. This requirement dictates the values of L_i and L_o used in this study. We find $L_i = 5$ is sufficient for all cases considered in this study. We vary L_o but verify that it is far downstream of computed perturbations.

Eigenvalues are computed using a modified Arnoldi iteration method[33]. In brief, repeated application of the relevant evolution operator, $\mathcal{A}(T)$ or $\mathcal{A}^*(\tau)\mathcal{A}(\tau)$, to a random starting vector $\mathbf{u_0}$ generates a Krylov sequence and subsequently an upper Hessenberg matrix, $\mathbf{H}$, which spans a subspace of the image of the operator. After relatively few iterations, the dominant eigenvalues of $\mathbf{H}$ converge to the dominant eigenvalues of $\mathcal{A}(T)$ or $\mathcal{A}^*(\tau)\mathcal{A}(\tau)$, thus allowing the important eigenvalues and eigenvectors to be computed at low computational cost and memory requirements.

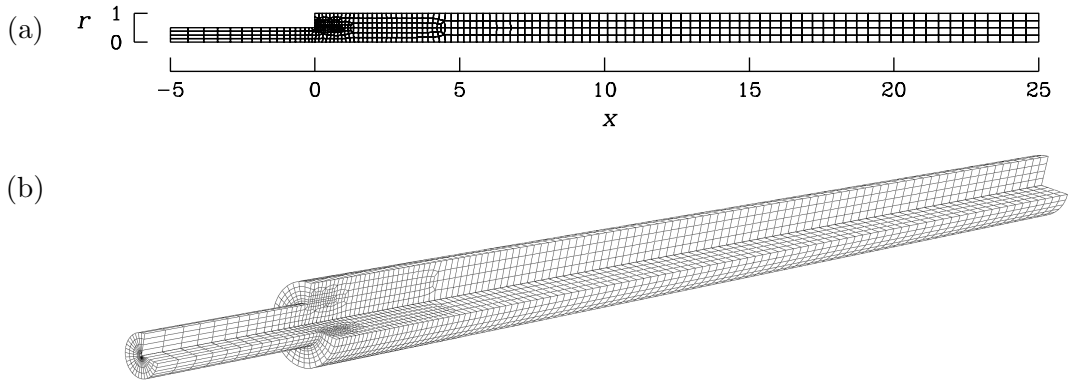

FIG. 3: A spectral element mesh used in this study. For the case illustrated there are 563 elements, an inflow length of $L_i = 5$ and an outflow length of $L_o = 25$. When required, meshes with more elements and outflow lengths up to $L_o = 75$ have been used. The two-dimensional mesh (a) used for linear analysis is extended to three dimensions (b) for non-linear analysis (DNS) where Fourier expansions are used in azimuth.

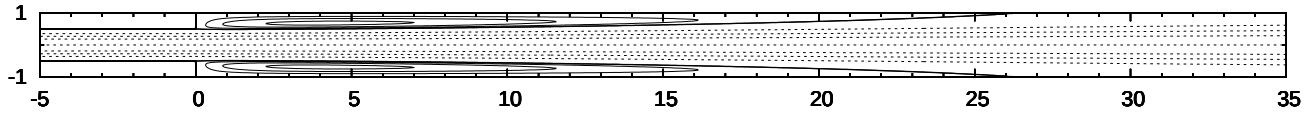

FIG. 4: Contour plot of the base-flow streamfunction at $Re = 600$, showing the separation and reattachment of the flow, and the recirculation region behind the expansion. Contours are drawn at intervals of 0.125 in the core of the flow, and at intervals of 0.02 in the recirculation region.

III. RESULTS

A. Base flows

We begin with a brief discussion of the steady, axisymmetric base flows. Figure 4 shows the streamfunction for a typical case, at Re=600. Streamlines of the high-speed core flow are drawn as dotted lines, while the separation streamline emanating from the expansion edge and the recirculation streamlines are drawn as solid lines. Contour level intervals for the streamfunction in the recirculation region and in the core region are distinctly different in order to better illustrate flow structure.

The base flows at all other Reynolds numbers in our study are qualitatively similar,

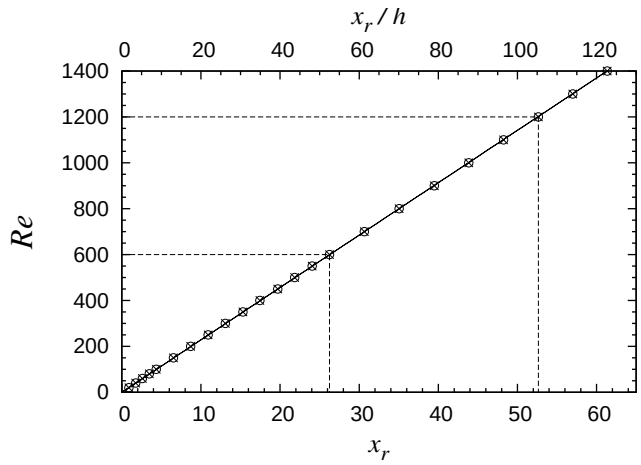

FIG. 5: Relationship between downstream reattachment point x_r and Reynolds number for base flows with a fully-developed inlet profile up to Re=1400. Points are the computed value of x_r and the solid line shows the best-fit proportionality given by $x_r/h = 0.0876\,Re$. The dotted lines indicate reattachment lengths for the base flows at Re=600 (corresponding to Fig. 4) and Re=1200.

differing primarily in length of the recirculation region. Figure 5 shows the relationship between the recirculation length, that is the downstream reattachment point denoted x_r, and Reynolds number for the base flows up to Re=1400. The recirculation length increases linearly with Re according to $x_r/h = 0.0876\,Re$. We believe this to be the most accurate study yet reported of recirculation length for the 1 to 2 expanding pipe. The constant of proportionality we obtain is slightly lower than that of Iribarne *et al.*[27], who report a linear relationship with a proportionality of 0.096 for a fully-developed inlet profile. However, our value matches the more recent experimental observations of Hammad *et al.*[3] who reported a value of 0.088.

B. Linear stability

For completeness we report in Table II the leading eigenvalues (those with largest real part) obtained from a linear stability analysis up to Re=1400. At least for Re from 600 to 1400 the leading eigenvalues all correspond to azimuthal modes with m=1 and only these eigenvalues are reported. The eigenvalues reported in Table II agree with those of Hall *et al.*[26] to within 0.3%. In all cases the leading eigenvalues are real and negative, and hence as stated at the outset, the axisymmetric base flow is linearly stable up to Re=1400. In fact

TABLE II: Leading eigenvalues for linear stability of flows in the 1 to 2 axisymmetric expansion for Reynolds numbers indicated. All values correspond to azimuthal mode number m=1. All are real and negative and hence the axisymmetric base flow is linearly stable up to at least $Re = 1400$.

Re	σ
600	-6.2388×10^{-3}
1000	-2.6827×10^{-3}
1400	-1.4571×10^{-3}

Hall *et al.*[26] determine that there are no positive eigenvalues to considerably higher Re.

C. Transient energy growth

Having established that the flow is linearly stable up to at least Re=1400, we turn to the determination of the most dangerous, that is energetic, transient dynamics. Recall that such a study involves not only the Reynolds number, but also the time horizon τ and the azimuthal mode number m. We begin by presenting results as a function of τ and m for a fixed value of Re and subsequently we consider the dependence on Re.

1. Dependence on azimuthal mode number

Figure 6 shows optimal growth envelopes $G(\tau)$ for perturbations in the axisymmetric (m=0) and first six non-axisymmetric modes (m=1 to 6) over a range of time horizons at a fixed Reynolds number of Re=600. In general, the greatest increase in energy is seen in the first azimuthal mode, m=1, which at this Reynolds number peaks at $\tau \simeq 50$, just at the right edge of the figure, and decreases for larger τ. The higher mode numbers exhibit less growth and peak at considerably smaller values of τ. For example, the m=2 growth envelope peaks at $\tau \simeq 19.5$ where the optimal growth there is an order of magnitude less than for the m=1 mode at the same value of τ and 1.5 orders of magnitude less than for the m=1 mode where it obtains its maximum.

There is generally a monotonic decrease in growth with increase in mode number, with two exceptions. The first is that the m=0, axisymmetric, mode growth envelope is qualitatively

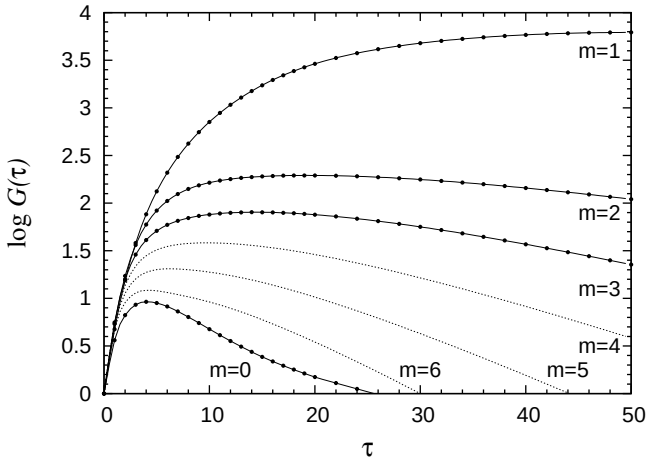

FIG. 6: Energy growth envelopes at Re=600 for azimuthal mode numbers (as indicated) up to m=6.

different from the others and in particular the growth peaks at a much earlier time horizon and has a much smaller value in comparison to any of the low-order, non-axisymmetric modes. The other exception to the dominance of m=1 is at small time horizons. Below $\tau \simeq 3$ the m=2 mode exhibits larger optimal growth than the m=1 mode, and below $\tau \simeq 2$ the m=3 mode exhibits larger optimal growth than the m=2 mode. (This can be clearly seen by enlarging the electronic version of Fig. 6.) We have not attempted to resolve the details and mode ordering at yet smaller values of τ. This modal behavior, where the m=1 mode dominates except for short time horizons, has also been reported for flows in parallel[36,37] and constricted[8] pipes.

The dominance of the energy growth for the m=1 mode is observed at all other Reynolds numbers in our study. Hence, for the remainder of the paper we shall mainly focus on the m=1 case. Some results will also be presented for the m=0 case since it is qualitatively different from the others and because it represents the strictly two-dimensional problem.

2. Reynolds number and time horizon

The dependence of the optimal growth on Reynolds number and time horizon is well summarized by contour plots of $G(\tau, Re)$. Figures 7(a) and (b) show such contour plots for m=1 and m=0 modes, respectively. Only contours with $G \geq 1$ are plotted and the no-growth contours, corresponding to $G = 1$, are emphasized by the thicker black curves.

TABLE III: Table of critical Reynolds numbers, Re_m^c, maximum growth values $G_m^{\max}$ and corresponding time horizons for maximum growth, $\tau_m^{\max}$ (for Re=600 and Re=1200 as indicated) for each of the first four azimuthal modes, m.

m	Re_m^c	$G_m^{\max}(600)$	$\tau_m^{\max}(600)$	$G_m^{\max}(1200)$	$\tau_m^{\max}(1200)$
0	64	9.20×10^0	4.4	2.32×10^1	6.2
1	26	6.23×10^3	50.1	3.77×10^6	106
2	38	1.95×10^2	19.5	7.59×10^2	34.1
3	54	8.05×10^1	14.6	3.17×10^2	28.3

To the right of the no-growth contours G is less than unity, meaning that the energy of any perturbation will be less than its initial energy at these values of τ.

The intersection of the no-growth contour with the Reynolds number axis is a saddle-point of the growth function in the $\tau - Re$ plane and indicates a critical Reynolds number, Re^c, above which energy growth is possible. This critical value depends on mode number m and so we define Re_m^c as the value of Re for which

$$\left.\frac{\partial G(\tau, Re_m^c)}{\partial \tau}\right|_{\tau=0} = 0.$$

For $Re > Re_m^c$, the growth envelope $G(\tau)$ for mode number m has positive slope at τ=0 and so $G(\tau) > 1$ for a least some values of τ. The smallest critical value occurs for m=1 with $Re_1^c = 26$. Values of Re_m^c for other m are also quite low and given in the second column of Table III.

As the Reynolds number increases perturbations with m=1 azimuthal structure can be amplified by large factors. Specifically, one can see in Fig. 7(a) that at Re=1200, perturbations are amplified by factors of over 10^6. Thus, even though the flow is linearly stable at Re=1200, it is capable of amplifying small perturbations to appreciable levels through strictly linear growth. In contrast to the m=1 modes, axisymmetric modes of Fig. 7(b) experience very limited growth and are confined to much shorter time horizons for all Re studied.

(a)

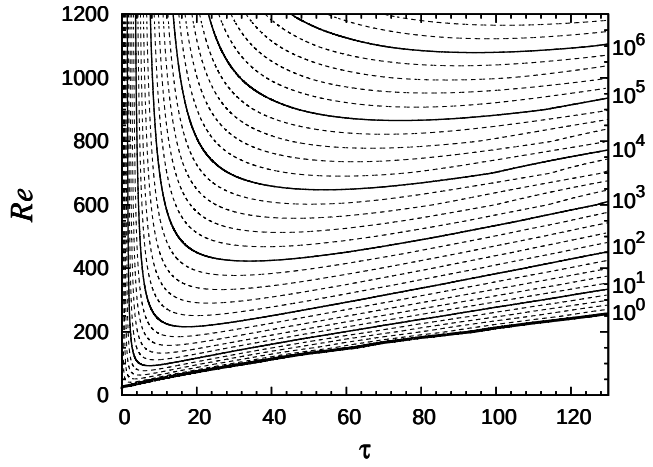

(b)

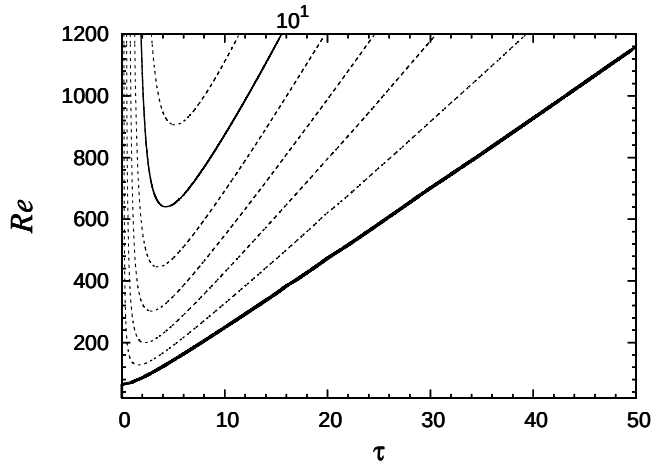

FIG. 7: Contours of optimal transient energy growth as a function of time horizon, τ, and Reynolds number for (a) azimuthal mode number m=1 and (b) azimuthal mode number m=0.

3. Time evolution of optimal perturbations

We now consider the time evolution of some optimal perturbations at Re=1200. Figure 8 shows the optimal growth envelope for Re=1200 and m=1, along with the transient energy evolution under the linearized Navier–Stokes equations from three different initial conditions. The initial perturbations are the computed optimal perturbations for three different values of τ as indicated. The case τ=110 is very nearly the initial condition giving the maximal energy growth at Re=1200. As is necessarily the case, each of these transient evolution curves touches the optimal growth envelope at its corresponding τ value, but otherwise they lie entirely below the envelope.

Figure 9 depicts the perturbation field evolving from the optimal initial condition for

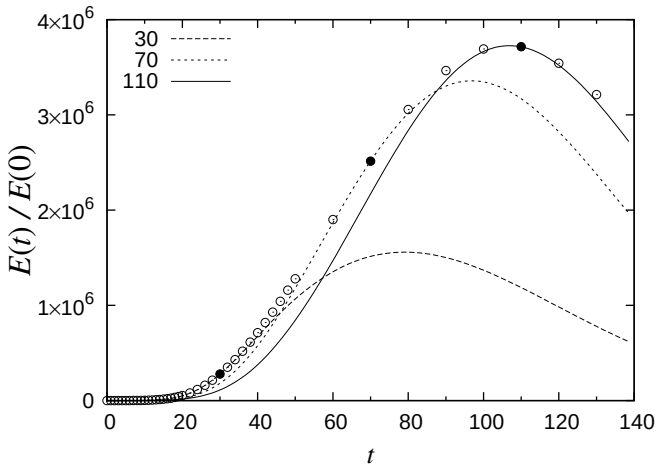

FIG. 8: Energy growth under linear evolution at Re=1200, m=1 for three different initial conditions corresponding to optimal perturbations at τ=30, 70 and 110. Circles denote the optimal growth envelope. Each linear evolution curve touches the envelope at its respective τ value, as indicated by a filled circle.

τ=110, (Re=1200, m=1). This evolution corresponds to the transient energy trajectory drawn with a solid line in Fig. 8. Owing to the small magnitude of the initial perturbation relative to its evolved state, we visualize the perturbation at early times differently from later times. Initially the perturbation is shown via a contour plot of the azimuthal velocity component u_θ in a planar cut through the geometry. Subsequent fields are visualized in terms of three-dimensional isosurfaces of azimuthal velocity. The evolving perturbation is plotted on a relatively small section of the computational domain every four time units until time 28. The perturbation is also plotted when it attains its maximum energy, at t=110. At this time the perturbation is well downstream of the expansion: the centroid of the perturbation energy lies at $x_c = 47.1$.

Unsurprisingly, the optimal initial perturbation is concentrated near the flow separation at the expansion from where it is subsequently advected by the base flow into the separated shear layer. In passing over the shear layer, chevron structures emerge in a packet, initially of very limited streamwise extent. After an initial rapid growth phase, the structure stabilizes as it approaches the time of peak growth after which the vortices at the rear of the structure begin to decay. The anti-symmetric appearance of the perturbation is a direct consequence of the m=1 azimuthal structure. Note that there is a characteristic axial wavelength of the

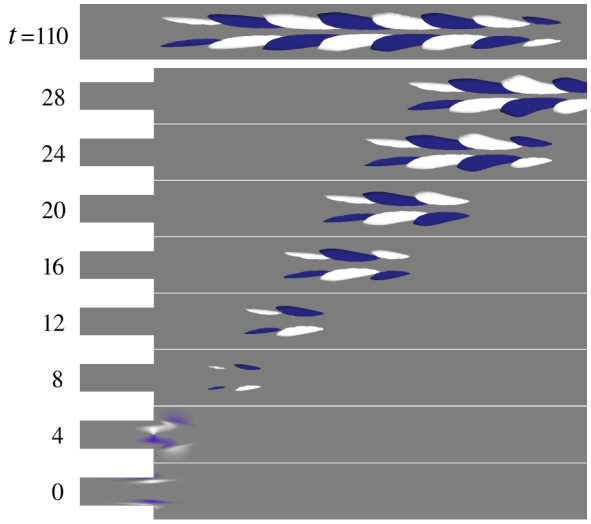

FIG. 9: Evolution of optimal initial disturbance in the m=1 mode visualized through contours/isosurfaces of azimuthal velocity at Re=1200 from $t = 0$ (bottom) in time intervals of four units in the spatial range $-2.5 \leq x \leq 15$. The top figure shows the evolved disturbance at its maximum growth. The spatial range is $36.5 \leq x \leq 54$ and the isosurface levels two orders of magnitude larger than in the lower part of the figure.

disturbance that is approximately preserved through the transient growth.

Transient behaviour of the optimal perturbation in m=0 at Re=1200 is illustrated through isosurfaces of radial velocity in Fig. 10. The initial disturbance is again concentrated around the step edge. Shortly afterwards it evolves into a set of toroidal rolls of alternating sign which advect downstream, first growing in energy up to $t \approx 6$, then decaying. Again note that the axial wavelength of the disturbance is preserved through this transient behaviour.

The physical nature of the perturbed shear layer for Re=1200, m=1 is illustrated in Fig. 11. The optimal perturbation at time of maximum energy growth is linearly combined with the base flow at a relative energy level of 5%. This combined state is visualized via an isosurface of azimuthal vorticity. The image suggests that the optimal perturbation manifests as a sinuous oscillation of the shear layer, as was also observed in the optimal growth analysis of flow in a stenotic pipe[8]. Note that the azimuthal orientation is arbitrary, due to rotational symmetry of the flow, and has been chosen here so as to emphasize the structure of the surface.

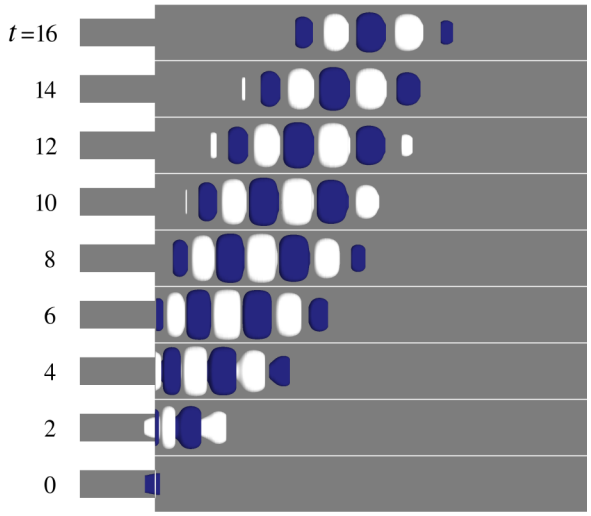

FIG. 10: Evolution of optimal initial disturbance in the m=0 mode visualized through isosurfaces of radial velocity at Re=1200 from $t = 0$ (bottom) in time intervals of two units in the spatial range $x \in [-2.5, 15]$.

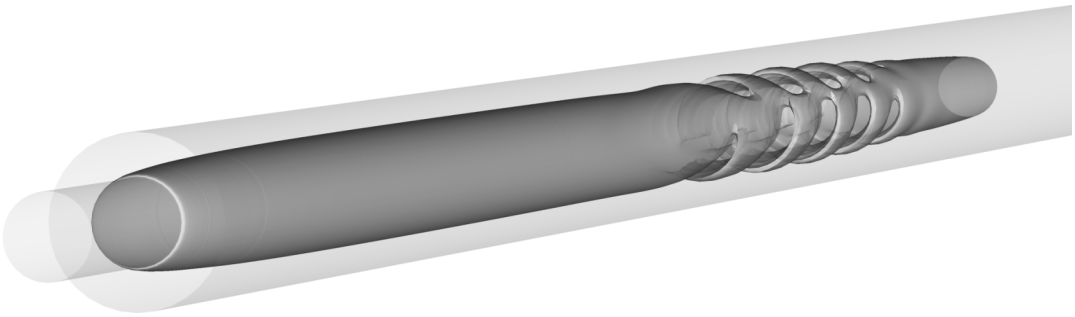

FIG. 11: Physical interpretation of the maximal disturbance at Re=1200. Shown is a linear superposition of the base flow with the optimal m=1 disturbance at the time of maximum growth, t=110. The disturbance has a relative energy magnitude of 5% compared to the base flow. The visualization is a semi-transparent isosurface of azimuthal vorticity at a level highlighting the separated shear layer.

4. Growth maxima

At a given Reynolds number, and for a specified azimuthal mode number m, the maximum of G over all time horizons τ is an important quantity. We thus define the maximum growth

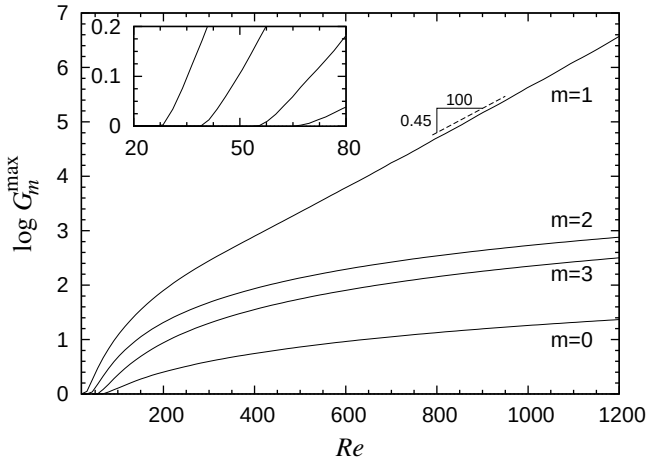

FIG. 12: Optimal energy growth, $G_m^{\max}$, as a function of Re for each of the first four azimuthal modes. Above $Re \approx 300$, $G_1^{\max}$ increases exponentially with Reynolds number at a rate of 0.41 orders of magnitude for each increase of 100 in Re. Inset shows detail at small Re. Curves intersect $\log G_m^{\max} = 0$ at the critical Reynolds number Re_m^c of each mode m.

and the corresponding time horizon as

$$G_m^{\max}(Re) = \max_{\tau} G(\tau, Re, m),$$
$$\tau_m^{\max}(Re) = \arg\max_{\tau} G(\tau, Re, m).$$

Table III includes the maximum growth and corresponding time horizons at representative Reynolds numbers of 600 and 1200.

The growth maxima are plotted in Fig. 12 as a function of Re for several values of m. Each curve emerges at the corresponding critical value Re_m^c. The figure highlights the significantly different magnitude of growth obtainable for m=1 perturbations compared with perturbations in other azimuthal mode numbers, particularly axisymmetric perturbations.

Beyond approximately Re=300, $\log G_1^{\max}(Re)$ is seen to be linear with Re indicating an exponential dependence of maximal growth on Reynolds number. This may also ultimately be true of the other broken symmetry perturbations at Reynolds numbers higher than those studied here. Similar exponential growth with Reynolds number has been observed for two other separated flows: flow over a backward-facing step[15] and steady flow in a stenotic pipe[8]. This exponential dependence is significantly different from the classic parallel flows, planar Couette flow[38] and straight pipe flow[36,38], for which the maximum transient growth increases only with the square of Reynolds number.

The form of evolved optimal perturbations at the time of maximal growth, $\tau_m^{\max}$, are

TABLE IV: Characteristics of the optimal perturbations at the time of maximum growth $\tau^{\max}$ for m=1 modes at Reynolds numbers indicated. Along with $\tau^{\max}$ the centroid location (x_c, r_c) of the evolved perturbation energy, as well as the local axial wavelength λ_x and temporal frequency St of the perturbation. At Re=600 the frequency spectrum is not sufficiently sharp to determine a value.

Re	$\tau^{\max}$	x_c	r_c	λ_x	St
600	50.1	21.3	0.40	4.6	-
800	69.0	29.9	0.40	4.2	0.082
1000	87.6	38.5	0.40	3.6	0.079
1200	106	47.1	0.40	3.3	0.081

expected to provide a good indication of what might be observed in a flow subject to small perturbations. See for example the perturbation at $t = 110$ in Fig. 9 and the combined state shown in Fig. 11. We shall address this in Sec. III D where we consider nonlinear simulations. Here we list in Table IV some pertinent characteristics of the optimal perturbation fields at the point of maximum growth for the case of m=1. For each Re, $\tau_m^{\max}$ is given, along with the centroid location (x_c, r_c) of the energy of the evolved perturbation, as well as the local axial wavelength λ_x and temporal frequency St of the perturbation. The wavelength of the evolved perturbation decreases slightly with Reynolds number, while the temporal frequency is essentially independent of Reynolds number. The non-zero radial location r_c is a consequence of the fact that the centroid is calculated from a Fourier mode, in the meridional semi-plane, and it represents the radial location where the disturbance is largest (if the energy centroid were calculated in physical space then r_c would be zero).

Fig. 13 shows x_c, the axial location of the perturbation energy centroid at maximal growth, together with the reattachment point of the base flow previously plotted in Fig. 5. One sees clearly that for $Re \gtrsim 500$ the optimal disturbance at its peak energy growth lies consistently about five diameters (10 step heights) upstream of the reattachment point of the base flow. This provides strong evidence that the separated shear layer is driving the growth of perturbations.

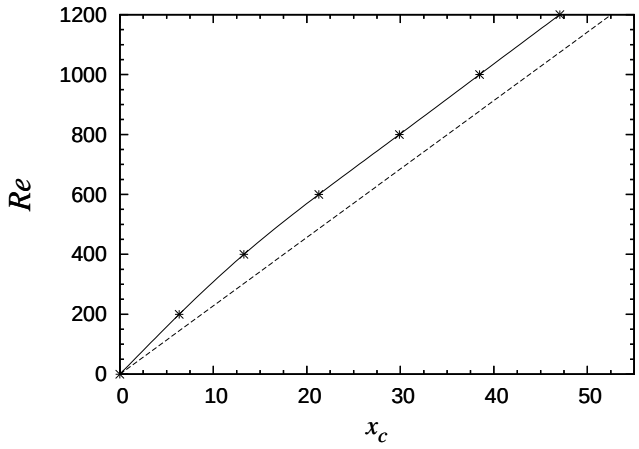

FIG. 13: Location of the centroid of the disturbance at its maximum growth (points connect by solid lines), compared with the location of the reattachment point (dashed line). The disturbance reaches its maximum approximately 5 diameters upstream of reattachment point.

5. Suboptimal growth

The optimal perturbations considered thus far are those which provide the maximum transient energy growth under linear evolution. However suboptimal perturbations can attain comparable energy, with the first sub-dominant perturbations in particular demonstrating growth on the same order of magnitude as the optimal perturbations. We have calculated suboptimal perturbations, and corresponding energy growth factors, by computing the subdominant eigenvalues and eigenmode of $\mathcal{A}^*(\tau)\mathcal{A}(\tau)$ in Eq. (7) by the Arnoldi method as described in Sec. II C

In Fig. 14 we show growth envelopes for the optimal and first three suboptimal perturbations at Re=600. A few additional suboptimal growth factors are plotted at $\tau = 50$. It is apparent that the growth envelopes are grouped in pairs. The first subdominant curve is very similar to the optimal envelope – it attains its growth maximum at nearly the same value of τ and with 80% the energy amplification of the optimal. Each of the second pair of suboptimal growth envelopes peaks at an earlier time horizon than for the first pair suggesting the eigenmodes undergo slightly different dynamics. These modes obtain about 30% of the optimal energy growth. The first eight leading eigenmodes at $\tau = 50$ indicates further pairing of modes. We have not resolved details of suboptimal dynamics further into the spectrum.

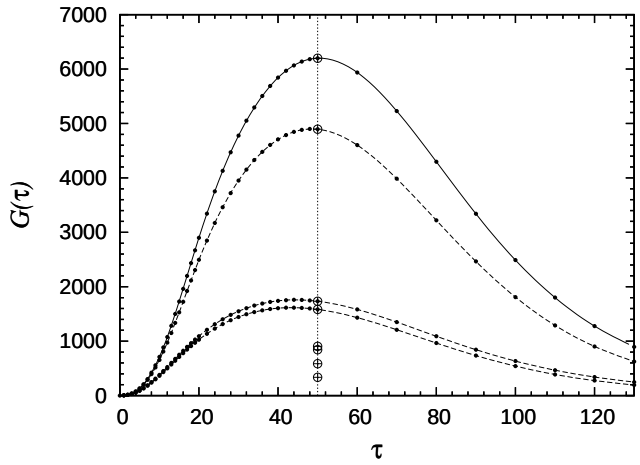

FIG. 14: Leading four growth envelopes for the optimal and suboptimal perturbations for the m=1 mode at Re=600. The circles on the dotted line at τ=50 show the first eight leading eigenvalues at the point of the peak optimal growth.

The perturbation fields themselves provide valuable insight into the pairing of growth envelopes. The azimuthal velocity of the four leading modes at $\tau = 50$ are visualized in Fig. 14. These fields have been obtained by evolving each (sub)optimal initial condition, each with the same energy norm, to time $t = 50$. Referring to Eq. (9), these are the first four left singular vectors of $\mathcal{A}(50)$ multiplied by the corresponding singular value. The isosurface levels are the same for all four modes.

The pairing of the eigenvalues is immediately apparent: the corresponding optimal modes come in pairs that are primarily related by a phase shift of $\pi/2$ relative to one another. This has been previously observed and discussed in the context of the planar backward-facing step[15]. For a truly streamwise invariant flow, such as for a straight pipe, the optimal modes necessarily come in pairs exactly related by a $\pi/2$ phase shift since the modes are trigonometric in the streamwise direction (sine and cosine pairs). Essentially, the expansion can be viewed as a breaking of streamwise translation symmetry of the flow. The breaking is very significant for the base flow since it gives rise to the separated shear layer which dominates the flow in the expanding pipe. However, the optimal perturbations see a flow with only a relatively weak broken streamwise symmetry and hence come in pairs with only slightly different dynamics and growth rates.

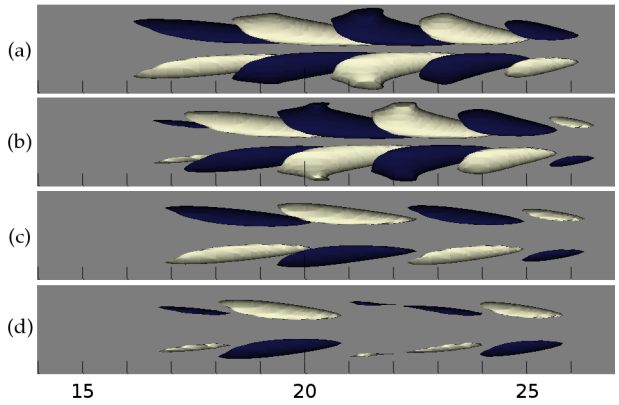

FIG. 15: Iso-surfaces of azimuthal velocity for the four leading perturbations at Re=600, m=1 evolved to time $t = 50$. (a) and (b) are the optimal and first sub-optimal modes. (c) and (d) are the next pair of sub-optimal modes. (See Fig. 14.)

D. Response to noise

To demonstrate the relevance of the linear growth computations to a real flow in the presence of small inlet noise, we have performed a limited number of full, three-dimensional direct numerical simulations with weak noise imposed on the inflow as described in Sec. II C. For each simulation, the initial state is the steady laminar flow at the given Reynolds number. Starting at time zero, noisy inflow boundary conditions are imposed.

In the first instance, we analyze the dynamics of the flow in terms of the modal energies over the full domain defined by

$$E_m(t) = \frac{1}{2}\int_\Omega ||\hat{\mathbf{u}}^m(t)||^2 \tag{12}$$

where $\hat{\mathbf{u}}^m$ is the m^{th} component of the azimuthal Fourier transformed velocity field. Figure 16 shows the evolution of modal energies at three values of Re. The axisymmetric component of the energy, E_0, is larger than all others and is off the scale of the figure. It starts at, and remains essentially unchanged from, the energy of the steady base flow.

In all cases, the energy of the m=1 mode grows within a short time as the effect of the noisy inflow condition propagates through the domain. For Re=600, the m=1 modal energy saturates above the noise floor of all other modes. It is nevertheless quite small. At Re=900, the m=1 modal energy saturates at 500 times the level of the noise floor. The m=2 modal energy is just barely distinguishable above the higher modes. At Re=1200, the first three modes are clearly visible with the m=1 modal energy more than four orders of magnitude

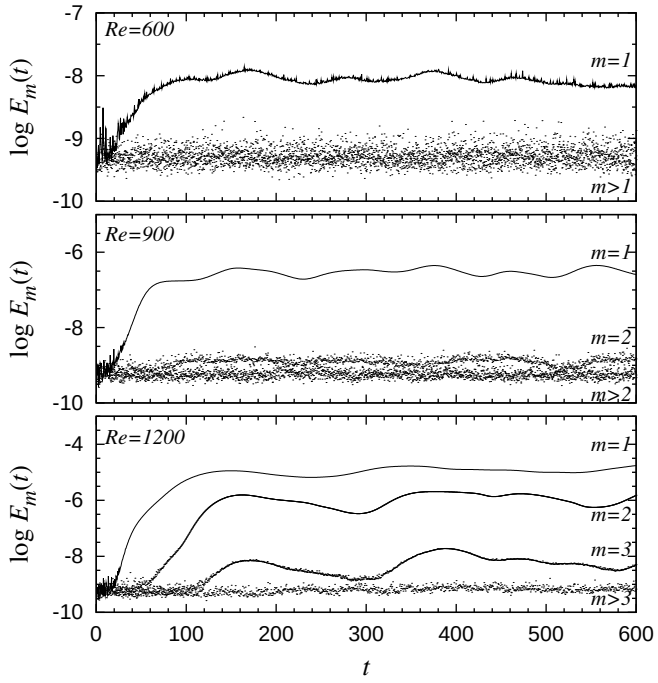

FIG. 16: Modal energy in a noisy inflow DNS of the expanding pipe flow at (a) Re=600, (b) Re=900, and (c) Re=1200. Modal energies visible above the noise floor of 10^{-9} are labeled. Initially the flow is the steady axisymmetric base flow. The axisymmetric energy E_0 is off the scale of the figure.

above the noise floor and approximately one order of magnitude above the m=2 mode. Some long period ($T \simeq 200$) dynamics may be present in the noise-driven flow at Re=1200, but we have not investigated these as they are outside the focus of our study.

The modal energies shown in Fig. 16 clearly confirm the dominant response of the m=1 mode as determined by the optimal growth analysis. Moreover, for the Reynolds numbers examined, the saturation value of the m=1 energy E_1 is consistent with exponential dependence on Re with half an order of magnitude for each Re increase of 100. This compares very favorably with the dependence of G_1^{max} on Re in Fig. 12.

Having established that a weak noisy inflow does in fact preferentially excite the m=1 mode, we proceed to examine the nature of the resulting flow. Figure 17 shows the optimal linear mode at Re=900 [Fig. 17(a)] and Re=1200 [Fig. 17(b)], together with instantaneous snapshots of the noise-driven flow at the corresponding Reynolds numbers. Specifically, the top half of each sub-figure shows the optimal perturbation, corresponding to m=1, at the

optimal time τ^{max}. Energy of the perturbation field is visualized. The bottom half of each sub-figure shows the three-dimensional flow at a representative time instant. The time is arbitrary except that it is chosen so that the phase of the nonlinear flow aligns with the phase of the optimal mode. For the nonlinear flow the axisymmetric modal energy (which dominates the flow) is removed and the energy in the remaining three-dimensional field in visualized in a semi-meridional plane (lower half of the pipe). Figure 18 further highlights the structure of nonlinear flow seen in Fig. 17(b) with contour plots of the three velocity components.

The most striking feature of the noise-driven nonlinear flow is that it exhibits precisely the same chevron structures as predicted by the transient growth analysis. The wavelengths of the fully nonlinear flow and the optimal perturbation are almost exactly the same. Moreover, while the structures in the noise-driven flow occupy a greater streamwise extent than the optimal perturbation, the location of the maximum in the nonlinear flow is well aligned with the location of the optimal. As the Reynolds number increases and the location of the optimum moves downstream, so does the location of the nonlinear maximum. There is one final interesting feature of the nonlinear state. Due to the rotational symmetry of the geometry, the m=1 structures may have any orientation in θ. Thus in the noise-driven flow the orientation of the chevron structures is not fixed but can, and does, vary in both space (seen in Fig. 18) and time.

The noise-driven nonlinear flow is time varying and depends on the noise level imposed at the inflow. We address these aspects briefly in Fig. 19. In Figs. 19(a)-(c) we capture the instantaneous state of the nonlinear flow at Re=900 at three times separated by 50 time units. The first plot, Fig. 19(a), is at the same time instant as Fig. 17(a). In this figure we plot kinetic energy as a function of x sampled along two rays down the length of the pipe. Both rays are at $r = 0.8$. One (solid) is at $\theta = 0$ and the other (dashed) is at $\theta = \pi/2$. Since the flow at Re=900 is dominated by m=1, it is sufficient to use only these two rays to sample the azimuthal structure of the flow. These kinetic energy profiles give a good representation of the instantaneous flow structures. Occasionally the nonlinear flow is relatively quiescent [as in Fig. 19(b)] and as can be seen in comparing Fig. 17(a) with Fig. 17(c), when structures are visible, their strength and location within the pipe vary to some extent.

For the same inlet noise, the structures occupy a much larger streamwise extent at Re=1200, Fig. 17(d), and they tend to be located further downstream. By reducing the

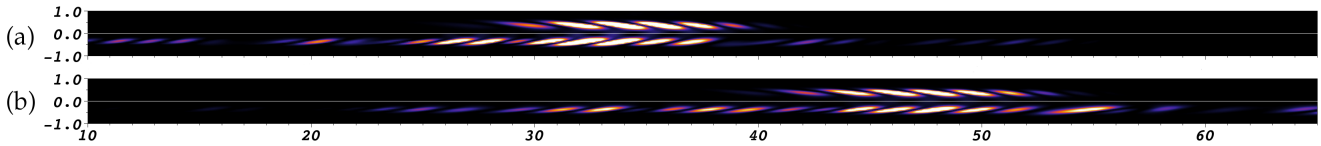

FIG. 17: Visualization of noise-driven flow and optimal perturbation at (a) Re=900, and (b) Re=1200, in the range $10 < x < 65$. The upper half of each pipe shows the m=1 optimal perturbation at the respective Reynolds number, evolved to the point of maximum growth. The lower half shows a snapshot of the noise-driven flow for comparison.

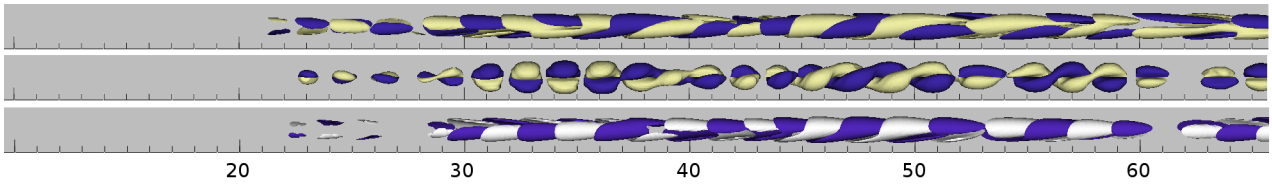

FIG. 18: Isosurfaces of streamwise (top), radial (middle) and azimuthal (bottom) velocity components for the noise-driven flow showing the downstream disturbance induced by the stochastic forcing at the same time instant as Fig. 17(b).

noise level of the input at Re=1200, the nonlinear state becomes more purely m=1 and the nonlinear structures tend to be more localized and shown in Fig. 17(e).

A profile comparison of the standard deviation of velocity components from the linear analysis and the noisy simulation is given in Fig. 20. The profiles for the noise-driven flow were obtained through temporal-azimuthal averaging of the flow and extracted through a radial line at x=100.0, while the linear profiles were attained through a streamwise averaging of the disturbance profile at its maximal evolution. The streamwise and radial profiles correlate to a high degree. The broader shape of the azimuthal profile from the noise-driven flow is probably due to the contribution of other modes in the system.

Finally, we have extracted important statistical properties of the flow with stochastic forcing. The frequency of the noise-driven flows are $St \approx 0.08$, in agreement with the optimal perturbations in Table. IV, but cannot be determined to better than one digit of accuracy. There are similar limitations on the wavelengths of the noise-driven flow and our opinion is that the visual comparison in Fig. 17 is probably more reliable. The centroids of the turbulent kinetic energy match those of the optimal perturbations to a reasonable degree in the streamwise direction, while matching almost exactly in cross-stream position.

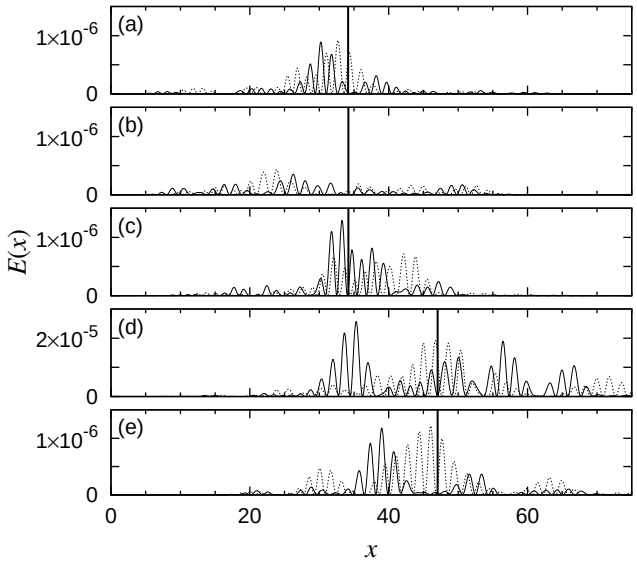

FIG. 19: Energy of noise-driven flow through the line $r = 0.8$ for the $\theta = 0$ (solid lines) and $\theta = \pi/2$ (dotted lines). (a)-(c) Re=900, (d) Re=1200, (e) Re=1200 at 1/4 the noise level of (d). Vertical lines indicate x_c, the centroid of the optimal linear perturbation at the corresponding value of Re.

Note that when comparing the centroid of the linear Fourier mode to that of the present noise-driven simulations, we use the centroid of a two-dimensional azimuthal-average of the turbulent kinetic energy.

IV. SUMMARY AND DISCUSSION

We have presented a numerical study of transient dynamics in an axisymmetric expanding pipe. As an important aside, we have first independently confirmed that the steady axisymmetric flow is indeed linearly stable up to Re=1400. We find that nevertheless at linear order perturbations are very strongly amplified in the region of the separated shear layer that extends downstream of the expansion. For example, at Re=1200 the energy of perturbations can be amplified by a factor of over 10^6. The initial disturbances giving maximal transient growth are localized in the vicinity of the pipe expansion and have azimuthal mode number m=1. Under linear evolution, these disturbances quickly evolve into packets of waves characterized by a chevron structure corresponding to a sinuous oscillation of the shear layer. These disturbances gain energy through an inflectional instability mechanism as they pass along the shear layer, reaching energetic maxima just upstream of the reattach-

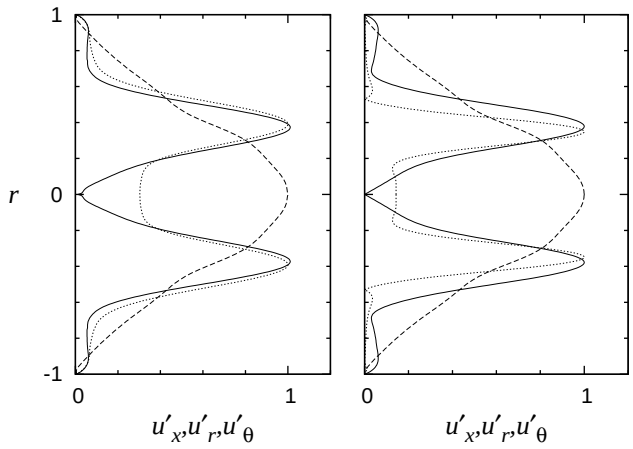

FIG. 20: Radial profiles of velocity component standard deviations comparing the noise-driven simulation (left) with the linear analysis (right). The three velocity components, each normalized to their peak value, are shown: streamwise (solid line), radial velocity (dashed line) and azimuthal velocity (dotted line).

ment point of the flow. Thereafter, disturbances advect downstream where they ultimately decay in the stable downstream pipe. Through direct numerical simulations we have established that the linear results do capture, quantitatively, most features seen in a fully three-dimensional nonlinear flow subjected to small Gaussian inlet noise. Thus we have not only quantified in detail the transient response of this flow but we have also demonstrated the importance of this type of linear analysis to flows that would commonly be described as convectively unstable, and thus noise amplifiers.

The expanding pipe flow shares many properties with other documented geometries, although there are also some important differences. The most similar example to the present one is found in a recent study of transient growth of disturbances to steady and pulsatile flows in a pipe with a smooth axisymmetric constriction[8]. Such flows have been the subject of extensive research[7,9,10,39,40] owing to the importance of the associated flows through arterial stenoses. The two other closely related flows are the planar backward-facing step[15,17] and the curved channel flow[32].

Probably the most significant similarity amongst all these separated flows is the dependence of growth rate on Reynolds number. In all cases, beyond some value of Re, the maximal growth $G^{\max}$ depends exponentially on Re. This exponential dependence is in stark contrast to parallel shear flows, such as straight pipes and channels, in which the maximum

growth typically scales only as the square of Reynolds number[36–38]. This highlights the very important difference between the transient growth studied here and that discussed extensively in parallel shear flows[41]. Here the transient growth is closely linked to the variation of the flow in the streamwise direction, as illustrated in Fig. 1. Physically, perturbations grow rapidly in the region of the shear layer driven by the inflectional velocity profile, but this growth is only transient because perturbations advect past the reattachment point and thereafter decay. Chomaz refers to convective non-normality[31] to distinguish these cases from the lift-up non-normality driving transient growth in parallel shear flows. See also Marquet *et al.*[42].

The exponents for different separated flows can be compared. In the present study, Fig. 12, $G^{\max}$ for the m=1 azimuthal mode increase at a rate of 0.41 orders of magnitude for each increase of 100 in Re. For convience in this discussion we denote this rate as $\alpha = 0.41/100$. In the study of stenotic flow[8] the rate is not explicitly reported but is obtainable from the available data. The rate is $\alpha = 1.23/100$. However, for the stenotic flow Re is based on the flow upstream of the stenosis. For comparison with the present work, the stenotic flow Re should be corrected upwards by a factor of 2 to account for the local Re at the stenosis. This gives a rate of increase of $G^{\max}$, again for the m=1 azimuthal mode, of $\alpha = 0.61/100$, quite close to that of the sudden axisymmetric expansion. In the study of the planar backward-facing step[15] the rate is stated explicitly giving $\alpha = 1.18/100$. This is the growth rate for strictly two-dimensional modes, but for the planar case three-dimensional effects are not very important. The Re for the backward-facing step is based on the centerline velocity. Correcting this downwards by a factor of 2/3 to convert to bulk velocity, $G^{\max}$ for the backward-facing step increases at a rate of $\alpha = 1.77/100$. This is faster than for the axisymmetric flows, but it is not altogether different.

Another point of comparison between the different separated flows is the downstream location of the optimal perturbation when it reaches its maximum growth. In all reported cases this downstream location grows linearly with Re. In the present study we find this location to be consistently 5 inlet diameters upstream of the reattachment point. In the steady stenotic case the location is consistently slightly downstream of the reattachment point, although not far from it. These findings are all consistent with the picture of a shear layer driven instability. Interestingly, this is very different from the case of the planar backward-facing step in which the optimal perturbation is well downstream of all separation and

reattachment points when it reaches its maximum growth. However, in the curved channel[32], the perturbation is located in the vicinity of the reattachment point at its growth maximum.

One can also consider the form of the optimal perturbations in different cases. Again, not surprisingly, the optimal modes found in the sudden expansion studied here are very similar to the optimal modes in the steady stenotic flow. In both cases the optimal perturbations have m=1 azimuthal structure and visually are nearly the same. (Compare Fig. 10 with Fig. 5 of Blackburn *et al.*[8].) On a more quantitative level one can compare the wavelengths in the two cases. From Table IV, at Re=800 the wavelength of the optimal disturbance at its maximal location is $\lambda = 4.2$. For the stenotic flow (in terms of equivalent Reynolds numbers and length scales) the wavelength is $\lambda = 3.7$. Taking into account the variation of wavelengths with Re and the fact that the conversion from the stenotic Reynolds number to the present one is not exact, these values are quite close. In any case, these wavelengths are significantly longer than those observed in the planar backward-facing step[15] and curved channel flow[32], in which the optimal modes have a roll structure whose wavelength is typically twice the outflow channel height.

One can likewise consider the Strouhal frequencies observed in various cases. Instead of attempting a detailed comparison, we take a slightly different approach following closely the discussion by Marquet *et al.*[32]. Noting that the perturbations are essentially packets of traveling waves, one can invoke the kinematic relationship $c = \lambda St$, equivalently $St = c/\lambda$, between the speed of a packet c, the wavelength, and the frequency. In the present study the bulk velocity in downstream pipe is 1/4 due to the 1 to 4 increase in cross-sectional area. Perturbations traveling at the bulk speed with typical wavelength, $\lambda = 3.6$ say at Re=1000, would be expected to have frequency $St = c/\lambda = 0.25/3.6 = 0.07$. This is essentially that observed. Marquet *et al.*[32] argue the same holds for the planar backward-facing step and the curved channel. In all cases the Strouhal frequencies are of comparable magnitude $St \sim 10^{-1}$; differences between the velocity scales in the different configurations hinders a more precise comparison.

Given that the dominant mechanism driving the growth of perturbations is surely inflectional instability of the shear layer, one could attempt to determine the frequency of growing perturbations from a local analysis of the numerically computed shear layer. This has been attempted for the backward-facing step and is further discussed by Marquet *et al.*[32]. Basically the difficulty is that, even ignoring that the flow is not parallel, the fre-

quency determined from a local analysis depends on the station at which the analysis is done and only the order of magnitude of the frequency is reliably determined. In reality the flow is far from parallel in the vicinity of the separation point and likewise the dynamics of perturbations is initially quite complex. See for example Fig. 9 at time 4.

We conclude with a brief discussion of related experiments. Our measurements of recirculation length give a linear dependence on Re according to $x_r/h = 0.0876\,Re$. This can be considered to be a perfect match to the proportionality 0.088 reported in experiments by Hammad *et al.*[3]. The connection between our computations and experiments with regard to the shear-layer oscillations is less satisfying at present. While there are several mentions of shear-layer oscillations in the experimental literature on the 1 to 2 expanding pipe, quantitative details are lacking. Typically oscillations are associated with the breakdown of the linear scaling of the recirculation length with Reynolds number[1,27,28] and there is no agreed value of the Reynolds number at which this occurs[4]. We believe that this is due to the fact that there is no linear instability to define such a threshold for oscillation and the onset of oscillations detectable in experiment will depend on factors such as the level of noise in the experiment. Oscillations observed in some experiments, for example by Sreenivasan and Strykowski[20] and Mullin *et al.*[5], are clearly of a very different character than the waves examined here. The oscillations found in these experiments have a much lower frequency, by more than an order of magnitude, than ours and are observed at Re above 1500.

There are two possible points of contact between calculations presented here and published experiments. The first is the work of Latornell and Pollard[4] on the expanding pipe. They report small sinusoidal waves appearing in the shear layer. At Re=750 these are observed to start at approximately 20 inlet diameters downstream of the expansion, which is consistent with our optimal growth results from Table IV. The other is the work of Griffith *et al.*[9] on flow in a stenotic geometry. They report shear-layer oscillations and in fact associate these with convective instability. Moreover, for a blockage of 0.75 (corresponding to a 1 to 2 expansion following the stenosis), they measure nondimensional oscillation periods roughly in the range of 0.2 to 0.3 for Reynolds numbers in the range 400 to 800. Converting to expanding pipe units, this gives Strouhal frequencies in the range 0.4 to 0.6 for Re between 800 and 1600. Although larger, these frequencies are of the same magnitude as those we obtain. Differences between the geometries could account for the discrepancy.

We hope that the detailed results presented here will motivate experimentalists to look

qualitatively at these transient dynamics in the future.

Acknowledgments

We are grateful to Edward Hall for sharing results from eigenvalue calculations on the expanding pipe flow. Computing facilities were provided by the UK Centre for Scientific Computing of the University of Warwick with support from the Science Research Investment Fund, and by the Australian National Computational Infrastructure National Facility, through MAS Grant D77.

---

[1] L. H. Back and E. J. Roschke, Shear-layer flow regimes and wave instabilities and reattachment lengths downstream of an abrupt circular channel expansion, ASME J. Appl. Mech **39**, 677 (1972).

[2] N. Furuichi, Y. Takeda, and M. Kumada, Spatial structure of the flow through an axisymmetric sudden expansion, Expts Fluids **34**, 643 (2003).

[3] K. J. Hammad, M. V. Otugen, and E. B. Arik, A piv study of the laminar axisymmetric sudden expansion flow, Expts Fluids **26**, 266 (1999).

[4] D. J. Latornell and A. Pollard, Some observations on the evolution of shear layer instabilities in laminar flow through axisymmetric sudden expansions, Phys. Fluids **29**, 2828 (1986).

[5] T. Mullin, J. R. T. Seddon, M. D. Mantle, and A. J. Sederman, Bifurcation phenomena in the flow through a sudden expansion in a circular pipe., Phys. Fluids **21**, 014110 (2009).

[6] R. G. Teyssandier and M. P. Wilson, An analysis of flow through sudden enlargements in pipes, J. Fluid Mech. **64**, 85 (1974).

[7] C. Bertolotti, V. Deplano, J. Fuseri, and P. Dupouy, Numerical and experimental models of post-operative realistic flows in stenosed coronary bypasses, J. Biomechanics **34**, 1049 (2001).

[8] H. M. Blackburn, S. J. Sherwin, and D. Barkley, Convective instability and transient growth in steady and pulsatile stenotic flows, J. Fluid Mech. **607**, 267 (2008).

[9] M. D. Griffith, T. Leweke, M. C. Thompson, and K. Hourigan, Steady inlet flow in stenotic geometries: convective and absolute instabilities, J. Fluid Mech. **616**, 111 (2008).

[10] S. J. Sherwin and H. M. Blackburn, Three-dimensional instabilities and transition of steady and pulsatile axisymmetric stenotic flows, J. Fluid Mech. **533**, 297 (2005).

[11] H. M. Blackburn and S. J. Sherwin, Instability modes and transition of pulsatile stenotic flow: Pulse-period dependence, J. Fluid Mech. **573**, 57 (2007).

[12] A. Acrivos and M. L. Schrader, Steady flow in a sudden expansion at high reynolds numbers, Phys. Fluids **25**, 923 (1982).

[13] F. Durst, J. C. F. Pereira, and C. Tropea, The plane symmetric sudden-expansion flow at low reynolds numbers, J. Fluid Mech. **248**, 567 (1993).

[14] R. M. Fearn, T. Mullin, and K. A. Cliffe, Nonlinear flow phenomena in a symmetric sudden expansion, J. Fluid Mech. **211**, 595 (1990).

[15] H. M. Blackburn, D. Barkley, and S. J. Sherwin, Convective instability and transient growth in flow over a backward-facing step, J. Fluid Mech. **603**, 271 (2008).

[16] L. Kaiktsis, G. E. Karniadakis, and S. A. Orszag, Onset of three-dimensionality, equilibria, and early transition in flow over a backward-facing step, J. Fluid Mech. **231**, 501 (1991).

[17] L. Kaiktsis, G. E. Karniadakis, and S. A. Orszag, Unsteadiness and convective instabilities in two-dimensional flow over a backward-facing step, J. Fluid Mech. **321**, 157 (1996).

[18] D. Barkley, M. G. M. Gomes, and R. D. Henderson, Three-dimensional instability in flow over a backward-facing step, J. Fluid Mech. **473**, 167 (2002).

J. F. Beaudoin, O. Cadot, J.-L. Aider, and J. E. Wesfreid, Three-dimensional stationary flow over a backward-facing step, Eur. J. Mech. B/Fluids **23**, 147 (2004).

[20] K. R. Sreenivasan and P. J. Strykowski, An instability associated with a sudden expansion in a pipe flow, Phys. Fluids **26**, 2766 (1983).

[19] E. O. Macagno and T.-K. Hung, Computational and experimenal study of a captive annular eddy, J. Fluid Mech. **28**, 43 (1967).

[21] D. Badekas and D. D. Knight, Eddy correlations for laminar axisymmetric sudden expansion flows, ASME J. Fluid Engng **114**, 119 (1992).

[22] A. Pollard, A contribution on the effects of inlet conditions when modelling stenoses using sudden expansions, J. Biomechanics **14**, 349 (1981).

[23] E. J. Roschke and L. H. Back, The influence of upstream conditions on flow reattachment lengths downstream of an abrupt circular channel expansion, J. Biomechanics **9**, 481 (1976).

[24] C. E. Tinney, M. N. Glauser, E. L. Eaton, and J. A. Taylor, Low-dimensional azimuthal

characteristics of suddenly expanding axisymmetric flows, J. Fluid Mech. **567**, 141 (2006).

[25] D. Drikakis, Bifurcation phenomena in incompressible sudden expansion flows, Phys. Fluids **9**, 76 (1997).

[26] K. A. Cliffe, E. J. C. Hall, and P. Houston, A numerical investigation of the bifurcation structure of flow in a pipe with a sudden expansion, (to be published).

[27] A. Iribarne, F. Frantisak, R. Hummel, and J. Smith, An experimental study of instabilities and other flow properties of a laminar pipe jet, A. I. Ch. E. J. **18**, 689 (1972).

[28] I. A. Feuerstein, G. K. Pike, and G. F. Round, Flow in an abrupt expansion as a model for biological mass transfer experiments, J. Biomechanics **8**, 41 (1975).

[29] P. Huerre and P. A. Monkewitz, Local and global instabilities in spatially developing flows, Annu. Rev. Fluid Mech. **22**, 473 (1990).

[30] C. Cossu and J. M. Chomaz, Global measures of local convective instabilities, Phys. Rev. Let. **78**, 4387 (1997).

[31] J.-M. Chomaz, Global instabilities in spatially developing flows: Non-normality and nonlinearity, Annu. Rev. Fluid Mech. **37**, 357 (2005).

[32] O. Marquet, D. Sipp, J. Chomaz, and L. Jacquin, Amplifier and resonator dynamics of a low-Reynolds number recirculation bubble in a global framework, J. Fluid Mech. **605**, 429 (2008).

[33] D. Barkley, H. M. Blackburn, and S. J. Sherwin, Direct optimal growth analysis for timesteppers, Intnl J. Num. Meth. Fluids **57**, 1437 (2008).

[34] L. S. Tuckerman and D. Barkley, in *Numerical Methods for Bifurcation Problems and Large-Scale Dynamical Systems*, edited by E. Doedel and L. S. Tuckerman, Springer, 2000, pp. 453–566.

[35] H. M. Blackburn and S. J. Sherwin, Formulation of a Galerkin spectral element–Fourier method for three-dimensional incompressible flows in cylindrical geometries, J. Comput. Phys. **197**, 759 (2004).

[36] L. Bergström, Optimal growth of small disturbances in pipe Poiseuille flow, Phys. Fluids **A5**, 2710 (1993).

[37] P. J. Schmid and D. S. Henningson, Optimal energy density growth in Hagen–Poiseuille flow, J. Fluid Mech. **277**, 197 (1994).

[38] S. C. Reddy and D. S. Henningson, Energy growth in viscous channel flows, J. Fluid Mech. **252**, 209 (1993).

[39] S. S. Varghese, S. H. Frankel, and P. F. Fischer, Direct numerical simulation of stenotic flows. part1. steady flow, J. Fluid Mech. **582**, 253 (2007).

[40] J. Vétel, A. Garon, D. Pelletier, and M.-I. Farinas, Asymmetry and transition to turbulence in a smooth axisymmetric constriction, J. Fluid Mech. **607**, 351 (2008).

[41] P. J. Schmid and D. S. Henningson, *Stability and Transition in Shear Flows*, Springer, 2001.

[42] O. Marquet, J. Chomaz, D. Sipp, J. Laurent, and M. Lombardi, Direct and adjoint global modes of a recirculation bubble: Lift-up and convective nonnormalities, J. Fluid Mech. **622**, 1 (2009).